

Feasibility of Single-Input Tracer Kinetic Modeling with Continuous-Time Formalism in Liver 4-Phase Dynamic Contrast-Enhanced CT

Sang Ho Lee¹(✉), Yasuji Ryu³, Koichi Hayano²,
and Hiroyuki Yoshida¹

¹ 3D Imaging Research, Department of Radiology,
Massachusetts General Hospital and Harvard Medical School,
25 New Chardon St., Suite 400C, Boston, MA 02114, USA
{lee.sangho,yoshida.hiro}@mgh.harvard.edu

² Division of Abdominal Imaging and Intervention, Department of Radiology,
Massachusetts General Hospital, 55 Fruit St., Boston, MA 02114, USA
khayano@partners.org

³ Department of Radiology, Graduate School of Medical Science,
Kanazawa University, 13-1 Takara-Machi, Kanazawa, Ishikawa 920-8641, Japan
ryu-kanazawa@umin.ac.jp

Abstract. The modeling of tracer kinetics with use of low-temporal-resolution data is of central importance for patient dose reduction in dynamic contrast-enhanced CT (DCE-CT) study. Tracer kinetic models of the liver vary according to the physiologic assumptions imposed on the model, and they can substantially differ in the ways how the input for blood supply and tissue compartments are modeled. In this study, single-input flow-limited (FL), Tofts-Kety (TK), extended TK (ETK), Hayton-Brady (HB), two compartment exchange (2CX), and adiabatic approximation to the tissue homogeneity (AATH) models were applied to the analysis of liver 4-phase DCE-CT data with fully continuous-time parameter formulation, including the bolus arrival time. The bolus arrival time for the 2CX and AATH models was described by modifying the vascular transport operator theory. Initial results indicate that single-input tracer kinetic modeling is feasible for distinguishing between hepatocellular carcinoma and normal liver parenchyma.

Keywords: Continuous-time tracer kinetic modeling · Bolus arrival time · Vascular transport operator · Four-phase dynamic contrast-enhanced CT

1 Introduction

Dynamic contrast-enhanced CT (DCE-CT) that involves intravenous administration of iodinated contrast agent (CA) can measure the vascular physiology of tumors through an analysis of the temporal changes of CT attenuation during sequential imaging. The fitting of a predefined compartmental model involves estimation of the values of kinetic parameters that provide a best fit to an observed concentration-time curve [1, 2].

A mathematical model is applied to the arterial and the tissue tracer concentration to estimate the physiologic parameters of interest.

Assessment of hemodynamic changes is particularly challenging for the liver due to its dual blood supply [3]. A dual-input model has potential to provide the physiologic proportions of blood supply to the liver tissue from the hepatic arterial system and from the portal venous system in vivo [4]. However, practical application of a dual-input model has various limitations. First, the hepatic artery may be difficult to locate, because it is thin and hardly visible on images. Therefore, the hepatic arterial input is generally approximated by sampling of the concentration-time curve at the abdominal aorta [4, 5, 6], which is a global input that supplies blood to the abdominal cavity. Thus, because the delay and dispersion of the CA to the aorta-hepatic artery pathway are prone to errors in the estimation of the flow [7], most of the currently developed dual-input liver models might not generate a precise physiological reality, although they would be physiologically more accurate than single-input models. Second, the low temporal resolution of 4-phase DCE-CT data may hamper the use of dual-input models with different physiologic scenarios because of high uncertainty in the intervals of data points that might contain mixed hepatic arterial and portal flow information. Furthermore, an additional parameter, such as arterial flow fraction in the dual-input models, can cause the total number of unknown parameters to exceed the effective degrees of freedom in measured data. Therefore, it may be necessary to make simplifying assumptions in order to reduce the number of parameters down to a manageable number, while providing a reasonable goodness-of-fit as well as enabling the study of different tracer kinetic models with varying degrees of complexity in the capillary-tissue system. Ultimately, there is a trade-off between computational cost and potential benefits of a precise model.

Tumor angiogenesis in the liver develops generally from the arterial blood supply rather than from the portal circulation, because the portal blood supply decreases with advancement of the tumor and eventually the tumor is fed mainly by arterial flow [8]. Thus, hepatic tumor circulation differs from the overall circulation pattern [9].

We performed a pilot study to evaluate six different single-input tracer kinetic models with the fundamental biophysical concepts and tracer kinetic principles of dynamic contrast-enhanced imaging: the flow-limited (FL) model [1], Tofts-Kety (TK) model [10], extended TK (ETK) model [11], Hayton-Brady (HB) model [12], two compartment exchange (2CX) model [13], and adiabatic approximation to the tissue homogeneity (AATH) model [14]. For parametric fitting of 4-phase DCE-CT data, the six models were extended to a fully continuous-time parameter formulation, including the bolus arrival time. Thus, the aim of this study was to investigate the discriminatory ability of each model between hepatocellular carcinoma (HCC) and normal liver parenchyma, and to demonstrate the potential of single-input tracer kinetic modeling in liver 4-phase DCE-CT.

2 Methods

2.1 Arterial Input Function

To derive the continuous formulation of each kinetic model in the time domain, first an arterial input function (AIF) needs to be modeled as a continuous-time functional form.

The AIF was acquired on the abdominal aorta with use of a sums-of-exponentials model from individual patients [15]. By imposing the bolus arrival time ($t_{\text{Lag,A}}$) in the artery [16], a functional form for the AIF model can be given by $C_A(t) = \{A_B(t - t_{\text{Lag,A}})e^{-\mu_B(t-t_{\text{Lag,A}})} + A_G(e^{-\mu_G(t-t_{\text{Lag,A}})} - e^{-\mu_B(t-t_{\text{Lag,A}})})\}u(t - t_{\text{Lag,A}})$, where $C_A(t)$ is the arterial blood concentration of CA (in g/ml), and $u(t)$ is the unit step function. The $A_B = a_B - a_B a_G / (\mu_B - \mu_G)$, $A_G = a_B a_G / (\mu_B - \mu_G)^2$, μ_B and μ_G are scaling constants that govern the height and shape of the AIF.

2.2 Continuous-Time Formulation of Tracer Kinetic Models

Once the AIF is modeled as a continuous-time functional form, an analytic solution for each kinetic model can be derived by incorporating the scaling constants of the AIF. Adopting the approach of a linear time-invariant system, the concentration of CA for the liver tissue, $C_T(t)$, can be described as a convolution integral between the impulse response function, $Q_T(t)$, and $C_A(t)$,

$$C_T(t) = Q_T(t) \otimes \frac{C_A(t)}{1 - H_{LV}}, \quad (1)$$

where H_{LV} is the hematocrit of blood in large vessels ($\cong 0.45$) [1], and \otimes denotes the convolution operator. All models considered here basically fall under this assumption. The impulse response functions $Q_T(t)$, for the six different models are given by

$$Q_{T,FL}(t) = v_P \frac{F}{V_P} e^{-\frac{v_P F}{v_D V_P} t}, \quad (2)$$

$$Q_{T,TK}(t) = v_P \frac{EF}{V_P} e^{-\frac{v_P EF}{v_1 V_P} t}, \quad (3)$$

$$Q_{T,ETK}(t) = v_P \delta(t) + v_P \frac{EF}{V_P} e^{-\frac{v_P EF}{v_1 V_P} t}, \quad (4)$$

$$Q_{T,HB}(t) = \frac{A_{HB}}{a - b} (e^{-bt} - e^{-at}), \quad (5)$$

$$Q_{T,2CX}(t) = v_P \frac{F}{V_P} \{Ae^{\alpha t} + (1 - A)e^{\beta t}\} \quad (6)$$

$$\text{with } \begin{pmatrix} \alpha \\ \beta \end{pmatrix} = \frac{1}{2} \left[-\left\{ \frac{F}{V_P} + \left(1 + \frac{v_P}{v_1}\right) \frac{PS}{V_P} \right\} \pm \sqrt{\left\{ \frac{F}{V_P} + \left(1 + \frac{v_P}{v_1}\right) \frac{PS}{V_P} \right\}^2 - 4 \frac{v_P F PS}{v_1 V_P V_P}} \right]$$

$$\text{and } A = \frac{\alpha + \left(1 + \frac{v_P}{v_1}\right) \frac{PS}{V_P}}{\alpha - \beta},$$

$$Q_{T,AATH}(t) = v_P \frac{F}{V_P} \left\{ u(t) + \left(E e^{-\frac{v_P EF}{v_1 V_P} (t - \frac{V_P}{F})} - 1 \right) u \left(t - \frac{V_P}{F} \right) \right\}, \quad (7)$$

where $Q_{T,FT}(t)$, $Q_{T,TK}(t)$, $Q_{T,ETK}(t)$, $Q_{T,HB}(t)$, $Q_{T,2CX}(t)$ and $Q_{T,AATH}(t)$ represent the $Q_T(t)$, for the FL, TK, ETK, HB, 2CX, and AATH models, respectively. Note that $\delta(t)$ is the Dirac delta function, v_P is the plasma volume fraction, v_1 is the interstitial volume fraction, $v_D = v_P + v_1$ is the relative distribution volume, V_P is the plasma volume (in ml), F is the plasma flow (in ml/min), PS is the permeability-surface area product (in ml/min), and $E = 1 - e^{-PS/F}$ is the extraction fraction, respectively. The A_{HB} , a and b are reparametrization of the compartmental variables [12]. To account for the difference in bolus arrival times between $C_A(t)$, and $C_T(t)$, a time lag (delay) to the liver tissue, $t_{Lag,T}$, can be imposed on either $C_A(t)$, or $Q_T(t)$ to calculate $C_T(t)$. For the AIF described above, the analytic forms of $C_T(t)$, are given explicitly for the six different models by

$$\begin{aligned} C_{T,FL}(t) &= Q_{T,FL}(t - t_{Lag,T}) \otimes \frac{C_A(t)}{1 - H_{LV}} \\ &= \frac{v_P}{1 - H_{LV}} \frac{F}{V_P} \left[\frac{a_B}{\left(\mu_B - \frac{v_P F}{v_D V_P} \right)^2} \left(1 + \frac{a_G}{\mu_G - \frac{v_P F}{v_D V_P}} \right) e^{-\frac{v_P F}{v_D V_P} (t - t_{BAT})} \right. \\ &\quad \left. + \frac{1}{\mu_B - \frac{v_P F}{v_D V_P}} \left\{ A_G - \frac{a_B - A_G (\mu_B - \mu_G)}{\mu_B - \frac{v_P F}{v_D V_P}} \right\} e^{-\mu_B (t - t_{BAT})} \right. \\ &\quad \left. - \frac{A_G}{\mu_G - \frac{v_P F}{v_D V_P}} e^{-\mu_G (t - t_{BAT})} - \frac{A_B}{\mu_B - \frac{v_P F}{v_D V_P}} (t - t_{BAT}) e^{-\mu_B (t - t_{BAT})} \right] u(t - t_{BAT}), \end{aligned} \quad (8)$$

$$\begin{aligned} C_{T,TK}(t) &= Q_{T,TK}(t - t_{Lag,T}) \otimes \frac{C_A(t)}{1 - H_{LV}} \\ &= \frac{v_P}{1 - H_{LV}} \frac{EF}{V_P} \left[\frac{a_B}{\left(\mu_B - \frac{v_P EF}{v_1 V_P} \right)^2} \left(1 + \frac{a_G}{\mu_G - \frac{v_P EF}{v_1 V_P}} \right) e^{-\frac{v_P EF}{v_1 V_P} (t - t_{BAT})} \right. \\ &\quad \left. + \frac{1}{\mu_B - \frac{v_P EF}{v_1 V_P}} \left\{ A_G - \frac{a_B - A_G (\mu_B - \mu_G)}{\mu_B - \frac{v_P EF}{v_1 V_P}} \right\} e^{-\mu_B (t - t_{BAT})} \right. \\ &\quad \left. - \frac{A_G}{\mu_G - \frac{v_P EF}{v_1 V_P}} e^{-\mu_G (t - t_{BAT})} - \frac{A_B}{\mu_B - \frac{v_P EF}{v_1 V_P}} (t - t_{BAT}) e^{-\mu_B (t - t_{BAT})} \right] u(t - t_{BAT}), \end{aligned} \quad (9)$$

$$C_{T,ETK}(t) = Q_{T,ETK}(t - t_{Lag,T}) \otimes \frac{C_A(t)}{1 - H_{LV}} = v_P \frac{C_A(t - t_{Lag,T})}{1 - H_{LV}} + C_{T,TK}(t) \quad (10)$$

$$\begin{aligned} C_{T,HB}(t) &= Q_{T,HB}(t - t_{Lag,T}) \otimes \frac{C_A(t)}{1 - H_{LV}} \\ &= \frac{A_{HB}}{1 - H_{LV}} \left[\frac{a_B}{(\mu_B - b)^2(a - b)} \left(1 + \frac{a_G}{\mu_G - b} \right) e^{-b(t - t_{BAT})} \right. \\ &\quad - \frac{a_B}{(\mu_B - a)^2(a - b)} \left(1 + \frac{a_G}{\mu_G - a} \right) e^{-a(t - t_{BAT})} \\ &\quad + \frac{1}{(\mu_B - a)(\mu_B - b)} \left\{ A_B \left(\frac{1}{\mu_B - a} + \frac{1}{\mu_B - b} \right) - A_G \right\} e^{-\mu_B(t - t_{BAT})} \\ &\quad + \frac{A_G}{(\mu_B - a)(\mu_B - b)} e^{-\mu_G(t - t_{BAT})} \\ &\quad \left. + \frac{A_B}{(\mu_B - a)(\mu_B - b)} (t - t_{BAT}) e^{-\mu_B(t - t_{BAT})} \right] u(t - t_{BAT}), \end{aligned} \quad (11)$$

$$\begin{aligned} C_{T,2CX}(t) &= Q_{T,2CX}(t - t_{Lag,T}) \otimes \frac{C_A(t)}{1 - H_{LV}} \\ &= \frac{v_P}{1 - H_{LV}} \frac{F}{V_P} \left[\frac{a_B A}{(\mu_B + \alpha)^2} \left(1 + \frac{a_G}{\mu_G + \alpha} \right) e^{\alpha(t - t_{BAT})} \right. \\ &\quad + \frac{a_B(1 - A)}{(\mu_B + \beta)^2} \left(1 + \frac{a_G}{\mu_G + \beta} \right) e^{\beta(t - t_{BAT})} \\ &\quad - \frac{1}{(\mu_B + \alpha)(\mu_B + \beta)} \\ &\quad \times \left[A_B \left\{ 1 - \frac{A(\alpha - \beta)}{\mu_B + \alpha} + \frac{(1 - A)(\alpha - \beta)}{\mu_B + \beta} + \frac{\mu_B + (1 - A)\alpha + A\beta}{\mu_B - \mu_G} \right\} \right. \\ &\quad \left. - \frac{a_B}{\mu_B - \mu_G} \{ \mu_B + \alpha - A(\alpha - \beta) \} \right] e^{-\mu_B(t - t_{BAT})} \\ &\quad - \frac{A_G}{\mu_G + \beta} \left\{ 1 - \frac{A(\alpha - \beta)}{\mu_G + \alpha} \right\} e^{-\mu_G(t - t_{BAT})} \\ &\quad \left. - \frac{A_B}{\mu_B + \beta} \left\{ 1 - \frac{A(\alpha - \beta)}{\mu_B + \alpha} \right\} (t - t_{BAT}) e^{-\mu_B(t - t_{BAT})} \right] u(t - t_{BAT}), \end{aligned} \quad (12)$$

$$\begin{aligned}
C_{T,AATH}(t) &= Q_{T,AATH}(t - t_{Lag,T}) \otimes \frac{C_A(t)}{1 - H_{LV}} \\
&= \frac{v_P}{1 - H_{LV}} \frac{F}{V_P} \left[\left\{ \frac{a_B}{\mu_B^2} \left(1 + \frac{a_G}{\mu_G} \right) - \frac{1}{\mu_B} \left(\frac{A_B}{\mu_B} - A_G \right) e^{-\mu_B(t-t_{BAT})} \right. \right. \\
&\quad \left. \left. - \frac{A_G}{\mu_G} e^{-\mu_G(t-t_{BAT})} - \frac{A_B}{\mu_B} (t - t_{BAT}) e^{-\mu_B(t-t_{BAT})} \right\} u(t - t_{BAT}) \right. \\
&\quad \left. - \left[\frac{a_B}{\mu_B^2} \left(1 + \frac{a_G}{\mu_G} \right) - \frac{a_B E}{\left(\mu_B - \frac{v_P EF}{v_1 V_P} \right)^2} \left(1 + \frac{a_G}{\mu_G - \frac{v_P EF}{v_1 V_P}} \right) e^{-\frac{v_P EF}{v_1 V_P} \left(t - \frac{v_P}{F} - t_{BAT} \right)} \right. \right. \\
&\quad \left. \left. - \frac{1}{\left(\mu_B - \frac{v_P EF}{v_1 V_P} \right)^2} \left[\left(1 - \frac{v_P EF}{v_1 V_P} \right)^2 \{ a_B - A_G (2\mu_B - \mu_G) \} \right. \right. \right. \\
&\quad \left. \left. \left. - E \left\{ a_B - A_G \left(2\mu_B - \mu_G - \frac{v_P EF}{v_1 V_P} \right) \right\} \right] \right] e^{-\mu_B \left(t - \frac{v_P}{F} - t_{BAT} \right)} \right. \\
&\quad \left. - A_G \left(\frac{1}{\mu_G} - \frac{E}{\mu_G - \frac{v_P EF}{v_1 V_P}} \right) e^{-\mu_G \left(t - \frac{v_P}{F} - t_{BAT} \right)} \right. \\
&\quad \left. \left. - A_B \left(\frac{1}{\mu_B} - \frac{E}{\mu_B - \frac{v_P EF}{v_1 V_P}} \right) \left(t - \frac{V_P}{F} - t_{BAT} \right) \right] e^{-\mu_B \left(t - \frac{v_P}{F} - t_{BAT} \right)} u \left(t - \frac{V_P}{F} - t_{BAT} \right) \right], \tag{13}
\end{aligned}$$

where $C_{T,FL}(t)$, $C_{T,TK}(t)$, $C_{T,ETK}(t)$, $C_{T,HB}(t)$, $C_{T,2CX}(t)$ and $C_{T,AATH}(t)$ represent $C_T(t)$ for the FL, TK, ETK, HB, 2CX, and AATH models, respectively. The $t_{BAT} = t_{Lag,A} + t_{Lag,T}$ is the bolus arrival time from the injection site of CA to the target tissue.

2.3 Kinetic Parameter Calculation

Model fitting was performed with a constrained nonlinear optimization algorithm based on MINPACK-1 [17], which yields the sum of squared errors as a measure of the goodness-of-fit [18]. The number of curve-fitting parameters was limited to at most four to avoid over-fitting to the data. The parameters that can be directly estimated by parametric fitting for each model are as follows: $\{F/V_P, v_P, v_1, t_{Lag,T}\}$ for the FL model, $\{EF/V_P, v_P, v_1, t_{Lag,T}\}$ for the TK and ETK models, $\{A_{HB}, a, b, t_{Lag,T}\}$ for the HB model, and $\{F/V_P, PS/V_P, v_P, v_1\}$ for the 2CX and AATH models. With these parameterizations, blood flow (BF) for the FL, 2CX, and AATH models, blood volume (BV) for all models except the HB model, mean transit time (MTT) for the FL, 2CX, and AATH models, permeability-surface area product (PS) for the 2CX and AATH models, extraction-flow product (EF) for all models except the HB model, and efflux rate constants (EF/V_1 for the TK, ETK, and AATH models, and PS/V_1 for the 2CX model, where V_1 is the interstitial volume (in ml)) can be computed according to: $BV = 100 \cdot V_P / \{(1 - H_{SV}) \cdot m\}$ (in ml/100 g), where H_{SV} is the hematocrit in small vessels ($\cong 0.25$) [1], and $m = \rho_T V_P / v_P$ is the mass of the tissue with density ρ_T ($= 1.04$ g/cm³ in the case of soft tissue), $BF = BV \cdot F / V_P$ (in ml/min/100 g),

$MTT = v_D V_P / (v_P F)$ (in min), $PS = (1 - H_{SV}) \cdot BV \cdot PS / V_P$ (in ml/min/100 g), $EF = (1 - H_{SV}) \cdot E \cdot BF$ (in ml/min/100 g), $EF/V_I = (v_P/v_I) \cdot EF/V_P$ (min^{-1}), and $PS/V_I = (v_P/v_I) \cdot PS/V_P$ (min^{-1}).

The $t_{Lag,T}$ for the 2CX and AATH models was modeled by modifying the vascular transport operator (VTO) theory [19], so that it could directly be estimated during the fitting procedure. Originally, the VTO theory was designed to estimate a pure delay of concentration-time curves at inflow and outflow on intravascular transport along a single path. The VTO consists of two components in series, a pure delay and a fourth-order linear differential operator that gives a dispersive delay. The parameters of the VTO are MTT and relative dispersion (RD), which is the standard deviation (SD) of the impulse response divided by MTT . To calculate SD at the target tissue, we used the tissue reside function, $R_T(t) = Q_T(t) \cdot V_P / (v_P F)$ instead of the impulse outflow response, $h_T(t) = -dR_T(t)/dt$ in [19], and then multiplied v_D into the SD to calculate the RD for each of the 2CX and AATH models. The RD and its corresponding $t_{Lag,T}$ for the 2CX and AATH models can be given by

$$\begin{aligned} RD_{2CX} &= v_D \sqrt{\int_0^{\infty} (\tau - MTT)^2 R_{T,2CX}(\tau) d\tau} \\ &= v_D \sqrt{-\frac{A}{\alpha^3} (2 + \alpha MTT (2 + \alpha MTT)) - \frac{1-A}{\beta^3} (2 + \beta MTT (2 + \beta MTT))}, \end{aligned} \quad (14)$$

$$\begin{aligned} RD_{AATH} &= v_D \sqrt{\int_0^{\infty} (\tau - MTT)^2 R_{T,AATH}(\tau) d\tau} \\ &= v_D \sqrt{\frac{V_P}{F} \left[\frac{1}{3} \left(\frac{V_P}{F} \right)^2 + MTT \left(MTT - \frac{V_P}{F} \right) \right.} \\ &\quad \left. + \frac{v_I}{v_P} \left(\frac{V_P}{EF} \right)^2 \left[2 \left(\frac{v_I}{v_P} \right)^2 + E \left(1 - \frac{F}{V_P} MTT \right) \left\{ E \left(1 - \frac{F}{V_P} MTT \right) + 2 \frac{v_I}{v_P} \right\} \right] \right]}, \end{aligned} \quad (15)$$

$$t_{Lag,T} = MTT \left(1 - \frac{RD}{0.48} \right), \quad (16)$$

where RD_{2CX} , RD_{AATH} , $R_{T,2CX}(t)$ and $R_{T,AATH}(t)$ are the RD and $R_T(t)$ for the 2CX and AATH models, respectively. The constant 0.48 is a maximum RD for the dispersiveness of the operator [19]. In case that $t_{Lag,T}$ was a negative value or a value greater than a stipulated threshold, it was assigned a value of 0 in the curve-fitting process so that it could converge into a new value.

2.4 Patients and DCE-CT Imaging

We investigated nine patient HCC cases to demonstrate clinical applicability of the six different single-input tracer kinetic models with the proposed continuous-time parameter formalism in 4-phase liver DCE-CT. The patients were scanned with a 64 multidetector CT scanner (LightSpeed VCT or Discovery CT750 HD; GE Medical Systems, Milwaukee, WI). A total of 1.7 ml/kg (80 to 135 ml) of nonionic iodinated CA (Iomeron; Eisai, Tokyo, 350 mg/ml) was injected with 30 s injection duration time at the rate of 3–5 ml/s and a volume as per 550–600 mgI/kg weight. The arterial-phase timing was determined with bolus tracking technology (Smart Prep; GE Healthcare), and scan was initiated 17 s after the preselected threshold of 200 HU was attained, with a region of interest (ROI) placed in the aorta above the celiac axis branching, where the $t_{\text{Lag,A}}$ was determined by observation of a snapshot to show the onset time of temporal enhancement in the aorta. The portal-venous phase and delayed phase initiated at 70 s and 150 s, respectively, after the preselected threshold of 200 HU was attained. In the patient cohort, $t_{\text{Lag,A}}$ ranged from 10 to 16 s, and the time when the preselected threshold of 200 HU was attained ranged from 14 to 24 s. The following CT parameters were used for obtaining volume data: 120 kVp, Auto mA, 16×0.625 mm detector collimation, 2.5 mm slice thickness, 95 to 120 slices, and a pitch of 1.

2.5 Image Processing and Analysis

To enhance contrast-to-noise ratios, DCE-CT images were denoised by use of multiple observations Gaussian process regression [20]. To reduce movement-induced artifacts, we coregistered each set of dynamic images with the portal-phase image as a template by using the Insight Segmentation and Registration Toolkit [21]. The registration was performed based on serial applications of 3D rigid, affine, and symmetric force Demons deformable registration methods with use of a multiresolution scheme [16]. For curve-fitting of the 4-phase DCE-CT data, 2D spatial filtering with a 5×5 pixel median kernel was applied on each DCE-CT sequence before extracting a voxel-level tissue concentration-time curve for fitting. ROIs were manually drawn by an experienced radiologist over a primary HCC and its adjacent normal tissue for each patient. Mean values in the ROIs (in total, 9 HCC and 9 normal tissue ROIs) were recorded for each parameter for each model for each patient. An example of fitting the voxel-level 4-phase DCE-CT data in HCC and normal tissue with the six different kinetic models is shown in Fig. 1.

2.6 Statistical Analysis

The predictable value of each parameter was evaluated by measuring the area under the receiver operating characteristic curve (A_Z). The Mann-Whitney (MW) test was used to test for differences in the mean values of each parameter between normal liver parenchyma and HCC ROIs. To assess the independent impact of each parameter on differentiation between HCC and normal liver parenchyma, binary logistic regression (BLR) analysis was performed with bootstrapping with 1000 replications. A P value <0.05 indicated a significant difference.

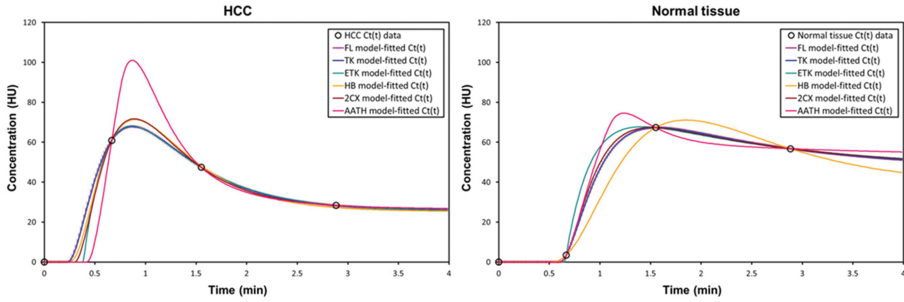


Fig. 1. Graphs illustrating examples of fitting the voxel-level 4-phase DCE-CT data with the FL, TK, ETK, HB, 2CX, and AATH models in the HCC (left) and normal liver tissue (right).

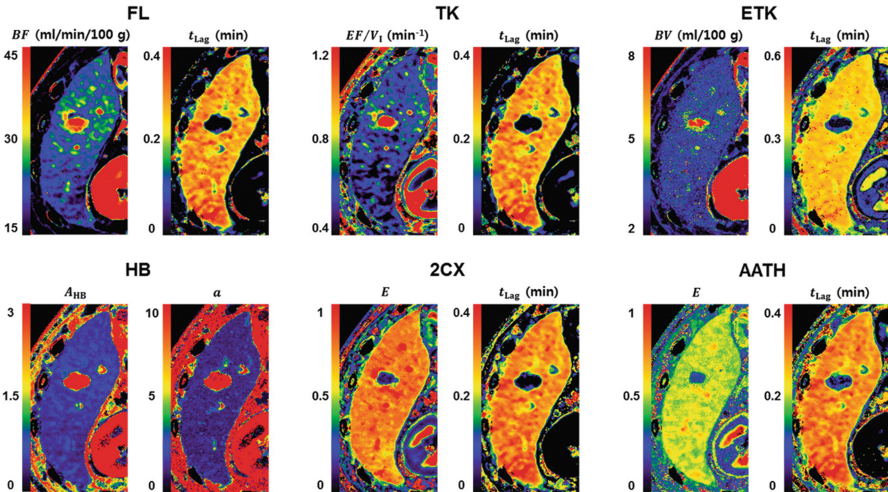


Fig. 2. Parametric maps obtained with six different tracer kinetic models for a patient with HCC. Each model displays two most significant parameters that yielded relatively higher discriminatory ability between HCC and normal liver tissue.

3 Results

Results of ROI analysis and comparison of the various hepatic microcirculatory parameters for the different models are shown in Table 1. In all of the applicable models, the ROIs of HCC showed increased BF and BV , earlier bolus arrival time $t_{Lag,T}$, shorter MTT , and smaller E than those of the normal liver tissue. The three parameters (i.e., A_{HB} , α , and b) for the HB model were all higher in the HCCs than in the normal liver tissue. The EF and EF/V_1 were higher in the HCC with the TK, ETK, and AATH models, whereas the EF and PS/V_1 were lower with the 2CX model. The v_1 was lower in the HCC with the FL, TK, ETK, and AATH models, whereas it was higher with the 2CX model. The PS was higher in the HCC with the AATH model,

Table 1. Statistics (mean ± SD) for ROI analysis of each parameter in the HCC and background liver tissue, and the corresponding results of MW and BLR tests.

Parameter	Model	Mean ± SD		A_z	P-value	
		HCC	Normal		MW	BLR
<i>BF</i> (ml/min/100 g)	FL	100.2 ± 84.53	40.52 ± 15.32	0.840	0.014	0.027
	2CX	93.49 ± 51.31	44.14 ± 13.09	0.938	0.001	0.011
	AATH	75.95 ± 40.71	41.19 ± 12.82	0.840	0.014	0.018
<i>BV</i> (ml/100 g)	FL	11.74 ± 7.681	6.958 ± 2.378	0.790	0.040	0.253
	TK	36.41 ± 22.86	20.44 ± 8.038	0.802	0.031	0.137
	ETK	11.70 ± 6.870	4.935 ± 1.053	0.975	<0.001	0.009
	2CX	24.97 ± 7.750	20.30 ± 4.343	0.654	0.297	0.056
	AATH	18.88 ± 6.872	14.78 ± 2.977	0.679	0.222	0.048
<i>MTT</i> (min)	FL	0.560 ± 0.338	1.366 ± 1.097	0.765	0.063	0.080
	2CX	0.658 ± 0.332	1.125 ± 0.783	0.679	0.222	0.060
	AATH	0.791 ± 0.421	1.316 ± 0.983	0.691	0.190	0.066
<i>PS</i> (ml/min/100 g)	2CX	29.01 ± 21.60	56.44 ± 45.14	0.765	0.063	0.113
	AATH	23.91 ± 16.41	18.46 ± 4.744	0.556	0.730	0.224
<i>EF</i> (ml/min/100 g)	TK	119.4 ± 156.1	29.70 ± 12.51	0.802	0.031	0.042
	ETK	38.27 ± 39.50	23.88 ± 8.052	0.519	0.931	0.154
	2CX	13.46 ± 11.68	19.11 ± 6.205	0.716	0.136	0.315
	AATH	16.85 ± 9.953	13.08 ± 2.833	0.593	0.546	0.209
<i>EF/V_I</i> or <i>PS/V_I</i> (min ⁻¹)	TK	4.947 ± 5.314	1.243 ± 0.708	0.827	0.019	0.024
	ETK	85.22 ± 159.9	1.197 ± 0.647	0.654	0.297	0.360
	2CX	181.7 ± 224.1	235.2 ± 321.8	0.531	0.963	0.675
	AATH	29.61 ± 62.90	0.985 ± 0.539	0.580	0.605	0.313
<i>v_I</i>	FL	0.173 ± 0.119	0.238 ± 0.081	0.753	0.077	0.345
	TK	0.265 ± 0.110	0.287 ± 0.071	0.605	0.489	0.665
	ETK	0.211 ± 0.146	0.262 ± 0.097	0.753	0.077	0.518
	2CX	0.179 ± 0.168	0.152 ± 0.132	0.556	0.730	0.695
	AATH	0.199 ± 0.154	0.209 ± 0.132	0.531	0.863	0.895
<i>E</i>	2CX	0.224 ± 0.108	0.605 ± 0.192	0.963	<0.001	0.002
	AATH	0.304 ± 0.093	0.438 ± 0.084	0.877	0.006	0.004
<i>A_{HB}</i>	HB	16.49 ± 11.19	3.119 ± 2.459	0.975	<0.001	0.004
<i>a</i>		14.63 ± 3.312	7.470 ± 5.046	0.877	0.006	0.004
<i>b</i>		5.690 ± 2.530	2.648 ± 1.320	0.864	0.008	0.006
<i>t_{Lag,T}</i> (min)	FL	0.028 ± 0.026	0.141 ± 0.087	0.926	0.001	0.004
	TK	0.034 ± 0.034	0.142 ± 0.087	0.877	0.006	0.004
	ETK	0.089 ± 0.049	0.271 ± 0.092	0.963	<0.001	0.021
	HB	0.021 ± 0.026	0.026 ± 0.043	0.531	0.863	0.778
	2CX	0.020 ± 0.024	0.156 ± 0.084	0.988	<0.001	0.002
	AATH	0.057 ± 0.036	0.181 ± 0.072	0.963	<0.001	0.002

Note—MW = Mann-Whitney, and BLR = binary logistic regression. Bold numbers indicate statistical significance ($P < 0.05$).

while it was lower with the 2CX model. Considering parameters with $A_Z > 0.95$ as well as statistical significance in both the MW and BLR tests, the ETK-model-derived BV ($A_Z = 0.975$, MW: $P < 0.001$, and BLR: $P = 0.009$) and $t_{Lag,T}$ ($A_Z = 0.963$, MW: $P < 0.001$, and BLR: $P = 0.021$), the HB-model-derived A_{HB} ($A_Z = 0.975$, MW: $P < 0.001$ BLR: $P = 0.004$), and the 2CX-model-derived E ($A_Z = 0.963$, MW: $P < 0.001$, and BLR: $P = 0.002$) and $t_{Lag,T}$ ($A_Z = 0.988$, MW: $P < 0.001$, and BLR: $P = 0.002$), and the AATH model-derived $t_{Lag,T}$ ($A_Z = 0.963$, MW: $P < 0.001$, and BLR: $P = 0.002$) led to a favorable outcome in this study. However, we note that all of the six different single-input models showed statistical significance in terms of discrimination between HCC and normal liver tissue. Parametric maps for two most significant parameters for each model that yielded relatively higher discriminatory ability between HCC and normal liver tissue are shown in Fig. 2.

4 Conclusion

We developed six different tracer kinetic models for 4-phase DCE-CT data analysis with fully continuous-time parameter formulation based on the linear time-invariant system, including the bolus arrival time. In particular, we enabled 4-phase data fitting with full two-compartment models such as the 2CX and AATH models by introducing the VTO theory. Because kinetic parameter values differ substantially among different models, the selection of a tracer kinetic model influences its discriminatory ability. The preliminary results indicate that single-input tracer kinetic modeling of the liver is feasible although the portal venous contribution to tumor perfusion is still an open question. Further work is encouraged to establish the clinical usefulness of the proposed approach in the imaging diagnosis and prognosis of HCC.

Acknowledgments. This study was supported in part by grant CA187877 from the National Cancer Institute at the National Institutes of Health.

References

1. Brix, G., Griebel, J., Kiessling, F., Wenz, F.: Tracer kinetic modelling of tumour angiogenesis based on dynamic contrast-enhanced CT and MRI measurements. *Eur. J. Nucl. Med. Mol. Imaging* **37**(Suppl 1), S30–S51 (2010)
2. Sourbron, S.P., Buckley, D.L.: Tracer kinetic modelling in MRI: Estimating perfusion and capillary permeability. *Phys. Med. Biol.* **57**, R1–R33 (2012)
3. Schenk Jr., W.G., McDonald, J.C., McDonald, K., Drapanas, T.: Direct measurement of hepatic blood flow in surgical patients: with related observations on hepatic flow dynamics in experimental animals. *Ann. Surg.* **156**, 463–471 (1962)
4. Koh, T.S., Thng, C.H., Lee, P.S., Hartono, S., Rumpel, H., Goh, B.C., Bisdas, S.: Hepatic metastases: In vivo assessment of perfusion parameters at dynamic contrast-enhanced MR imaging with dual-input two-compartment tracer kinetics model. *Radiology* **249**, 307–320 (2008)

5. Koh, T.S., Thng, C.H., Hartono, S., Kwek, J.W., Khoo, J.B., Miyazaki, K., Collins, D.J., Orton, M.R., Leach, M.O., Lewington, V., Koh, D.M.: Dynamic contrast-enhanced MRI of neuroendocrine hepatic metastases: A feasibility study using a dual-input two-compartment model. *Magn. Reson. Med.* **65**, 250–260 (2011)
6. Materne, R., Smith, A.M., Peeters, F., Dehoux, J.P., Keyeux, A., Horsmans, Y., Van Beers, B.E.: Assessment of hepatic perfusion parameters with dynamic MRI. *Magn. Reson. Med.* **47**, 135–142 (2002)
7. Calamante, F., Willats, L., Gadian, D.G., Connelly, A.: Bolus delay and dispersion in perfusion MRI: Implications for tissue predictor models in stroke. *Magn. Reson. Med.* **55**, 1180–1185 (2006)
8. Matsui, O.: Detection and characterization of hepatocellular carcinoma by imaging. *Clin. Gastroenterol. Hepatol.* **3**, S136–S140 (2005)
9. Miles, K.A.: Functional computed tomography in oncology. *Eur. J. Cancer* **38**, 2079–2084 (2002)
10. Tofts, P.S., Brix, G., Buckley, D.L., Evelhoch, J.L., Henderson, E., Knopp, M.V., Larsson, H.B., Lee, T.Y., Mayr, N.A., Parker, G.J., Port, R.E., Taylor, J., Weisskoff, R.M.: Estimating kinetic parameters from dynamic contrast-enhanced T(1)-weighted MRI of a diffusable tracer: Standardized quantities and symbols. *J. Magn. Reson. Imag.* **10**, 223–232 (1999)
11. Sourbron, S.P., Buckley, D.L.: On the scope and interpretation of the Tofts models for DCE-MRI. *Magn. Reson. Med.* **66**, 735–745 (2011)
12. Hayton, P., Brady, M., Tarassenko, L., Moore, N.: Analysis of dynamic MR breast images using a model of contrast enhancement. *Med. Image Anal.* **1**, 207–224 (1997)
13. Brix, G., Bahner, M.L., Hoffmann, U., Horvath, A., Schreiber, W.: Regional blood flow, capillary permeability, and compartmental volumes: Measurement with dynamic CT—initial experience. *Radiology* **210**, 269–276 (1999)
14. St Lawrence, K.S., Lee, T.Y.: An adiabatic approximation to the tissue homogeneity model for water exchange in the brain: I. Theoretical derivation. *J. Cereb. Blood Flow Metab.* **18**, 1365–1377 (1998)
15. Orton, M.R., d’Arcy, J.A., Walker-Samuel, S., Hawkes, D.J., Atkinson, D., Collins, D.J., Leach, M.O.: Computationally efficient vascular input function models for quantitative kinetic modelling using DCE-MRI. *Phys. Med. Biol.* **53**, 1225–1239 (2008)
16. Lee, S.H., Ryu, Y., Hayano, K., Yoshida, H.: Continuous-time flow-limited modeling by convolution area property and differentiation product rule in 4-Phase liver dynamic contrast-enhanced CT. In: Yoshida, H., Warfield, S., Vannier, M.W. (eds.) *Abdominal Imaging 2013*. LNCS, vol. 8198, pp. 259–269. Springer, Heidelberg (2013)
17. Moré, J.J., Garbow, B.S., Hillstom, K.E.: User Guide for MINPACK-1 (1980)
18. Markwardt, C.B.: Non-linear least squares fitting in IDL with MPFIT. In: *Proceedings of Astronomical Data Analysis Software and Systems XVIII*, Quebec, Canada, ASP Conference Series, vol. 411, p. 251 (2009)
19. King, R.B., Deussen, A., Raymond, G.M., Bassingthwaight, J.B.: A vascular transport operator. *Am. J. Physiol.* **265**, H2196–H2208 (1993)
20. Zhu, F., Carpenter, T., Rodriguez Gonzalez, D., Atkinson, M., Wardlaw, J.: Computed tomography perfusion imaging denoising using gaussian process regression. *Phys. Med. Biol.* **57**, N183–N198 (2012)
21. Ibanez, L., Schroeder, W., Ng, L., Cates, J.: *The ITK Software Guide*. Kitware, Inc., Clifton Park (2005)